

Non-optical Water Quality Retrieval from Zhuhai-1 OHS Hyperspectral Images in Taipu River

Yukun Yukun¹, Yaojen Tu¹, Wenpeng Lin¹, Weiyue Li¹, and Qianwen Cheng¹

¹Shanghai Normal University

December 14, 2022

Abstract

Hyperspectral remote sensing is thought to be a useful technology for assessing the condition of inland waters. However, non-optically active water quality parameters are rarely explored in hyperspectral remote sensing applications, despite they are highly valued in the aquatic environment condition. This study intends to evaluate the performance of non-optically active water quality parameters using Zhuhai-1 hyperspectral imagery. Focusing on total nitrogen (TN), total phosphorus (TP), ammonia nitrogen (NH₃-N) and nitrate-nitrogen (NO₃-N) in Taipu River, we constructed empirical models to evaluate the precision of water quality inversion from OHS by comparing with Sentinel-2, and determined the sensitive bands of different water quality parameters. The final results showed that the polynomial model based on OHS had the greatest potential in retrieving TN, TP and NH₃-N concentration, and the R² was 0.9678, 0.7924, 0.7682 respectively. The combination of R(510)/R(820) and R(700)/R(806), R(940)/R(820) and R(806)/R(926), R(709)/R(806) and R(746)/R(620) were most sensitive to TN, TP and NH₃-N respectively. The OHS and Sentinel-2 both had potential in retrieving NO₃-N. The R² was 0.9791 from OHS and was 0.9513 from Sentinel-2. The sensitive bands of NO₃-N were R(596)/R(665) and R(466)/R(580) from OHS, and Red Edge3/Blue and SWIR1/Blue from Sentinel-2. We also analyzed the drivers of the spatial distribution of water quality in Taipu River, the results showed negative impacts of farmland and urban land on water quality, and beneficial impacts of forest land on water quality. This study represented a promising step in hyperspectral remote sensing for retrieving inland non-optically active water quality parameters utilizing Zhuhai-1.

Hosted file

951400_0_art_file_10509883_rmgqxx.docx available at <https://authorea.com/users/566147/articles/612942-non-optical-water-quality-retrieval-from-zhuhai-1-ohs-hyperspectral-images-in-taipu-river>

1 Non-optical Water Quality Retrieval from Zhuhai-1 OHS Hyperspectral Images 2 in Taipu River

3 Yukun Lin^{a,b}, Yaojen Tu^{a,b,*}, Wenpeng Lin^{a,b,*}, Weiyue Li^{a,b}, Qianwen Cheng^{a,b}

4 a School of Environmental and Geographical Sciences, Shanghai Normal University, Shanghai
5 200234, China

6 b Yangtze River Delta Urban Wetland Ecosystem National Field Scientific Observation and
7 Research Station, Shanghai 200234, China

8 Abstract

9 Hyperspectral remote sensing is thought to be a useful technology for assessing the condition
10 of inland waters. However, non-optically active water quality parameters are rarely explored in
11 hyperspectral remote sensing applications, despite they are highly valued in the aquatic
12 environment condition. This study intends to evaluate the performance of non-optically active
13 water quality parameters using Zhuhai-1 OHS hyperspectral imagery. Focusing on total nitrogen
14 (TN), total phosphorus (TP), ammonia nitrogen (NH₃-N) and nitrate-nitrogen (NO₃-N) in Taipu
15 River, we constructed empirical models to evaluate the precision of water quality inversion from
16 OHS by comparing with Sentinel-2, and determined the sensitive bands of different water quality
17 parameters. The final results showed that the polynomial model based on OHS had the greatest
18 potential in retrieving TN, TP and NH₃-N concentration, and the R² was 0.9678, 0.7924, 0.7682
19 respectively. The combination of R(510)/R(820) and R(700)/R(806), R(940)/R(820) and
20 R(806)/R(926), R(709)/R(806) and R(746)/R(620) were most sensitive to TN, TP and NH₃-N
21 respectively. The OHS and Sentinel-2 both had potential in retrieving NO₃-N. The R² was 0.9791
22 from OHS and was 0.9513 from Sentinel-2. The sensitive bands of NO₃-N were R(596)/R(665)
23 and R(466)/R(580) from OHS, and Red Edge3/Blue and SWIR1/Blue from Sentinel-2. We also
24 analyzed the drivers of the spatial distribution of water quality in the Taipu River based on
25 redundancy analysis (RDA), the results showed negative impacts of farmland and urban land on
26 water quality, and beneficial impacts of forest land on water quality. This study represented a
27 promising first step in hyperspectral remote sensing for retrieving inland non-optically active
28 water quality parameters utilizing Zhuhai-1.

29 Keywords: Zhuhai-1 satellite, non-optical parameters, water quality, Taipu River, empirical model

30 I. INTRODUCTION

31 The Taipu River serves as a major drinking water supply route for the Yangtze River Delta
32 Ecology and Greenery Integration Development Demonstration Zone in China. The upstream is
33 linked to the East Taihu Lake Water Source, while the downstream is linked to Shanghai Jinze
34 Reservoir and the Jiashan Changbaidang Drinking Water Source Protection Area(H. Zhu, 2018). It
35 serves as a key canal for flood discharge and shipping, moreover, serves as a source of drinkable
36 water, which needs to meet strict criteria for water quality and ecological balance. Along the Taipu
37 River, the dense populations and considerable industries such as chemical, textile, printing and
38 dyeing, polyester, will deteriorate water quality(Y. Wang et al., 2021). Recently, pollution
39 occurrences in the Taipu River have sparked considerable concern. Therefore, analyzing the
40 spatiotemporal distribution features of the Taipu River's water quality is increasingly critical.

41 Four significant non-optical parameters, TN, TP, NH₃-N, and NO₃-N, have been extensively
42 investigated to represent the eutrophication of rivers and lakes, which will cause a critical water
43 pollution issue in many countries like degrading functioning and endangering water security (X.
44 Chen et al., 2018; Liang et al., 2018; Lv & Wu, 2021; Mararakanye et al., 2022). Traditionally,
45 in-situ measurements and the collection of water samples are the major approaches for monitoring
46 water quality. Even if these measurements are accurate for a specific area, they cannot provide a
47 regional perspective on water quality (Ross et al., 2019; D. Sun et al., 2014). In order to represent
48 the spatial distribution and seasonal changes in water quality components, remote sensing
49 technology has been adopted due to the benefits of spatial and temporal coverage (Kallio et al.,
50 2001; K. Shi et al., 2018; Xu et al., 2016). Different sensors with visible and infrared wavelengths
51 may be utilized to monitor water quality due to high-frequency data collecting and large-scale
52 coverage.

53 Generally, the spectral resolution of data sources for water quality retrieval can be classified
54 into two categories: multispectral data and hyperspectral data (H. Yang et al., 2022). In the field of
55 multispectral water quality retrieval, many scholars monitor the TN and TP using National
56 Oceanic and Atmospheric Administration (NOAA) Advanced Very High Resolution Radiometer
57 (AVHRR) imagery (Y. Wang et al., 2016), Landsat series data (H. Guo et al., 2022), MODIS data
58 (Arman, 2021), IKONOS imagery (J. Liu et al., 2015) and Sentinel-2 imagery (H. W. Guo et al.,
59 2021). The accuracy (R^2) range of TN/TP in references is from 0.36 to 0.87 and 0.59 to 0.96
60 individually. The scenes of high-resolution multispectral SPOT-5 (Satellite Pour l'Observation de
61 la Terre) data (X. L. Wang et al., 2011), Landsat-8 OLI satellite data (C. Liu et al., 2019),
62 Sentinel-2 imagery (Dong et al., 2020) and Unmanned Aerial Vehicle (UAV) multispectral data (B.
63 T. Chen et al., 2021) were used to establish the relationship between the surface reflectance and
64 NH₃-N. The accuracy (R^2) range of NH₃-N in references is from 0.69 to 0.88. The multispectral
65 technology has no relevant results in the monitoring of NO₃-N in inland rivers. Generally, due to
66 spectral resolution limitations, the overall precision of multispectral remote sensing water quality
67 is relatively low.

68 In the field of hyperspectral water quality retrieval, hyperspectral remote sensing data from
69 the ground-based and proximal hyperspectral imager (Q. Cao et al., 2022; X. Sun et al., 2022), the
70 handheld Analytical Spectral Devices (ASD) field spectrometer (S. Wang et al., 2022) and the
71 UAV equipped with a hyperspectral imaging sensor (Song et al., 2014), were applied to water
72 quality retrieval of TN and TP. The accuracy (R^2) is higher than multispectral with the range of
73 TN/TP in references from 0.59 to 0.90 and 0.73 to 0.93 individually. The ground-based
74 hyperspectral data (Q. Cao et al., 2022) and UAV-borne hyperspectral imagery (Wang et al., 2021)
75 were used to estimate water quality retrieval of NH₃-N. The accuracy (R^2) is higher than
76 multispectral with the range from 0.83 to 0.95. The ground-based hyperspectral data was used to
77 estimate water quality retrieval of NO₃-N. The accuracy (R^2) range of NO₃-N in reference is 0.77.
78 However, focusing just on the spectrum makes it challenging to understand the spatial distribution
79 of water quality along the whole river channel (Wang et al., 2021). In addition, non-satellite
80 remote sensing data sources that rely on aircraft measurements are more expensive and requires
81 superb UAV operation skills. Moreover, hyperspectral satellites can also solve the problems of
82 synonyms spectrum in multispectral data due to its numerous bands (Y. Cao et al., 2018). These
83 days, the Orbita Hyperspectral Satellites (OHS) with fine spectral, spatial, and temporal resolution

84 are available. However, the applicability of monitoring inland water quality parameters utilizing
85 OHS data has not been well investigated, particularly for the non-optically active water quality
86 parameters.

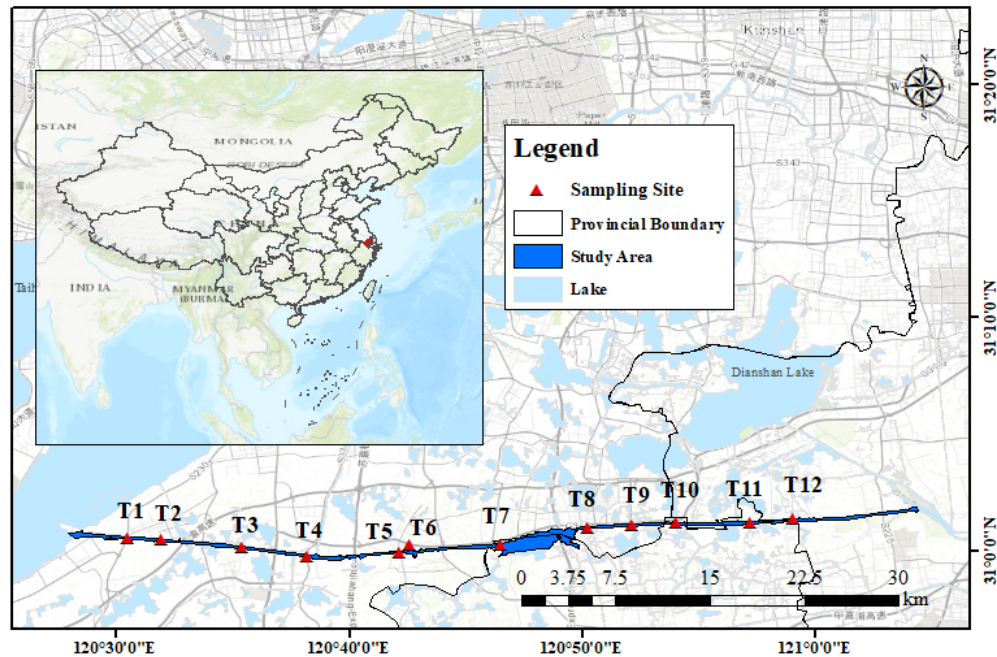
87 The study aims to retrieve TN, TP, NH₃-N and NO₃-N concentrations in the Taipu River from
88 OHS data, as well as to investigate the performance of the empirical model based on the single
89 band and band ratio. In the study, the case study area and relevant data sets were introduced
90 initially. Then, the waterbody was extracted and the cloud and dark surface in the images were
91 detected and removed. Next, we presented four empirical band arithmetic algorithms (linear,
92 logarithmic, exponential and polynomial) for TN, TP, NH₃-N and NO₃-N retrieval. The
93 performances on the Sentinel-2A multispectral image and OHS hyperspectral images were
94 compared and the sensitive features were investigated respectively. The optimal model with the
95 best-performed image were used to create maps of water quality concentration in the Taipu River.
96 The results will be explained and discussed then. Finally, we draw some conclusions.

97 **II MATERIALS**

98 **A. Study Sites and in Situ Data**

99 The Taipu River is a part of the Taihu Lake Basin's river network. Additionally, it is also
100 strongly connected to the surrounding water network, which comprises 205 small to medium-sized
101 lakes, and is impacted by the influx of tributaries on both sides of the river. The length and width
102 of the Taipu River are 57.2 kilometers and 200 meters, respectively. The flow rate is 0.6 m/s on
103 average, and the flow is about 300 m³/s (Yao et al., 2015). Along this canal are tens of thousands
104 of textile factories as well as 95 centralized sewage disposal facilities. (Yao et al., 2014).
105 Therefore, Taipu River is a typical area for water quality research.

106 As shown in Figure 1, a total of 12 in-situ samples of water quality parameters were collected
107 in Taipu River. The field measurements include total nitrogen (TN), total phosphorus (TP),
108 ammonia nitrogen (NH₃-N) and nitrate-nitrogen (NO₃-N). The samples are all concentrated at the
109 intersection of the major streams and regional functional zones. The sampling points were
110 measured on July 7, 2021, since the synchronized OHS and Sentinel-2 images corresponded to the
111 Taipu River field experiments were acquired in July 6, 2021 and July 7, 2021 respectively.



112

113 Figure 1 Map of sampling sites for water quality inversion of Taipu River

114 **B. Remote Sensing Data**

115 The Zhuhai-1 mission, developed by Zhuhai Orbita Control Engineering Ltd.
 116 (<https://www.myorbita.net/>), was China's first commercial microsatellite constellation. The
 117 Zhuhai-1 mission includes 34 microsatellites: 12 video satellites (OVS-1/2/3/4), two high spatial
 118 resolution satellites (OUS), two radar satellites (SAR), eight infrared satellites (OIS), and ten
 119 hyperspectral satellites (OHS)(Qin et al., 2022). The Orbita Hyperspectral Satellites (OHS)
 120 comprise 32 bands with a wavelength range of 400 to 1000 nm, a spatial resolution of 10 m, and a
 121 spectral resolution of 2.5 nm. To date, the single OHS has a temporal resolution of 6 days, and the
 122 combined temporal resolution of 8 OHSs is reduced to about 1 day(Zhong et al., 2021). The OHS
 123 has significant promise for monitoring inland water quality due to its high spatial, spectral, and
 124 temporal resolutions. The preprocessing of OHS includes band combination, radiometric
 125 calibration, atmospheric correction, and orthorectification, which converts the raw images into
 126 surface reflectance with precise geometric positioning, laying the groundwork for the subsequent
 127 inversion of water quality parameters. All the preprocessing steps are completed in ENVI 5.3.

128 Sentinel-2 Level-1C (L1C) MSI data could be downloaded from Sentinels Scientific Data
 129 Hub (<https://scihub.copernicus.eu/>). Sentinel-2 comprises 13 spectral bands with a wavelength
 130 range of 430 to 2190 nm. The 5 days revisit time of the twin Sentinel-2 satellites is crucial because
 131 of the water quality changes caused by weather condition. The spatial resolution of Sentinel-2 is
 132 10m, 20m and 60m, which means even small river and lakes can be studied(Toming et al., 2016).
 133 The Sen2Cor plug-in in the SNAP (SeNtinel Application Platform) toolbox was used for
 134 atmospheric correction to obtain the reflectance level images. The images then resampled to 20m
 135 resolution utilizing the Sentinel-2 Resampling technique also provided by SNAP Toolbox(J. Shi et
 136 al., 2022). Table 1 summarized the key technological characteristics of the OHS and Senitnel-2.

Table 1 Center Wavelength and Spatial Resolution of OHS and Sentinel-2

Channel	OHS			Sentinel-2		
	Center wavelength (nm)	Band Number	Spatial resolution (m)	Center wavelength (nm)	Band Number	Spatial resolution (m)
Blue	443	B01	10	490	b2	10
	466	B02				
	490	B03				
Green	500	B04	10	560	b3	10
	510	B05				
	531	B06				
	550	B07				
	560	B08				
Red	580	B09	10	665	b4	10
	596	B10				
	620	B11				
	640	B12				
	665	B13				
Red Edge1	670	B14	10	705	b5	20
	686	B15				
	700	B16				
	709	B17				
Red Edge2	730	B18	10	740	b6	20
	746	B19				
Red Edge3	760	B20	10	783	b7	20
	776	B21				
	780	B22				
NIR (Sentinel-2)	806	B23	10	842	b8	10
	820	B24				
	833	B25				
Narrow NIR (Sentinel-2)	850	B26	10	865	b8a	20
	865	B27				
NIR (OHS)	880	B28	10	—	—	—
	896	B29				
	910	B30				
	926	B31				
	940	B32				
SWIR1	—	—	—	1610	b11	20
SWIR2	—	—	—	2190	b12	20

138 **III. METHODS**

139 **A. Waterbody Extraction**

140 The water mask of Taipu River was derived from a vector dataset, the Open Street Map
141 (OSM). OSM contains a huge amount of objects related to water and it is widely used in
142 environmental applications including the extraction of rivers, lakes, and shoreline boundaries for
143 hydrological analysis(Donchyts et al., 2016; Marshak et al., 2020). In this study, we merged all the
144 OSM vectors in Taipu River into a single layer and corrected the typographic errors through the
145 visual interpretation process of the OHS image. All the steps are performed in ArcMap 10.7.

146 **B. Cloud Detection and Dark Surface Detection**

147 The spectral bands of optical sensors are substantially impacted by clouds(Irish et al., 2006),
148 in addition, the calculation of spectral indices might suffer from their existence(Huete et al., 2002).
149 Therefore, identifying clouds in optical images is often a prerequisite for their use(Z. Zhu et al.,
150 2015). There was no cloud in the OHS image but sparse cloud in the Sentinel-2 image. Fmask 4.0
151 was applied to detect cloud for Sentinel-2 image by integrating auxiliary data, new cloud
152 probabilities, and novel spectral-contextual features, which outperformed Sen2Cor 2.5.5 in terms
153 of overall accuracy by 7%(Qiu et al., 2019).

154 Taipu River, the urban surface water, is easily affected by noise in heterogeneous urban
155 scenes, such as soil, roadways and cloud shadows(X. Yang et al., 2018). The water index, AWEIsh,
156 was calculated to enhance the difference between water and non-water bodies(X. Yang et al.,
157 2018). The AWEIsh tends to have positive values for water bodies, whereas negative values for
158 soil and cloud shadows. The empirical threshold of 0.214 was adopted in this study. The
159 waterbody of Sentinel-2 was conducted by combination of cloud detection result and non-water
160 dark surfaces .The result of cloud/cloud shadow removal is presented in Figure 2.



162 Figure 2 Water mask for the true color composite image (Red, green and blue bands) of Sentinel-2 scenarios (water
163 mask in blue).

164 **C. Water Quality Inversion**

165 The water quality inversion are following three steps. First, from each sample point in the
166 Taipu River, the mean value of 3×3 cloud-free pixels were calculated for avoiding noise
167 effectively. Then, the single band and band ratio of OHS and Sentinel-2 were selected to create the
168 effective spectral information expression and to provide a framework for the qualitative and
169 quantitative assessment of water quality. Finally, linear regression model was established by linear,
170 logarithmic, exponential and polynomial, which was constructed by Formulas (1)-(4). Model
171 inversion was mainly realized through MATLAB 2021a.

172 $Linear \propto a \times R_{rs} + b$ (1)

173 $Logarithmic \propto a \times \log_{10} R_{rs} + b$ (2)

174 $Exponential \propto a \times e^{b \times R_{rs}}$ (3)

175 $Polynomial \propto a \times R_{rs}(\lambda) + b \times R_{rs} + c$ (4)

176 where R_{rs} represents band or band ratio of remote sensing images and a, b and c are the fitting
 177 coefficients.

178 **D. Validation and Evaluation**

179 The predictive performance of the linear regression model is primarily determined by the
 180 square of the correlation coefficient (R^2) and the Root Mean Squared Error (RMSE), which are
 181 calculated between the measured values and predicted values. The best models for assessing water
 182 quality are those with the highest R^2 value and the lowest RMSE. The followings are the equations
 183 of measurements:

184 $RMSE = \sqrt{\sum_{i=1}^n (y_i - y'_i)^2 / n}$ (5)

185 $R^2 = 1 - \sum_{i=1}^n (y_i - y'_i)^2 / \sum_{i=1}^n (y_i - \bar{y}_i)^2$ (6)

186 where y_i and y'_i are the observed and predicted value for the i th observation; \bar{y}_i is the average
 187 observed value; n is the number of validation samples.

188 **IV. RESULTS**

189 **A. Analysis of Measured Water Quality**

190 The statistics of the measured water quality in this experiment are listed in Table 2, which
 191 summarizes the measured water quality parameters in this experiment. The range of TN
 192 concentrations was from 0.972 to 2.192 mg/L, and the mean (\pm standard deviation) was $1.457 \pm$
 193 0.371 mg/L. According to the “Surface Water Environmental Quality Standard” (GB 3838-2002)
 194 in China, the average value of TN met the requirement of water class IV. The range of TP
 195 concentrations was from 0.03 to 0.14 mg/L, and the mean (\pm standard deviation) was 0.075 ± 0.034
 196 mg/L. The average value of TP met the requirement of water class III. The range of NH_3 -N
 197 concentrations was from 0.25 to 1.45 mg/L, and the mean (\pm standard deviation) was 0.537 ± 0.307
 198 mg/L. The average value of NH_3 -N met the requirement of water class III. Overall the water
 199 quality was below Class IV. Tthe overall water quality of the Taipu River tends to be the same as
 200 previous years.

201 Table 2 Summary of water quality concentrations of Taipu River sampling points.

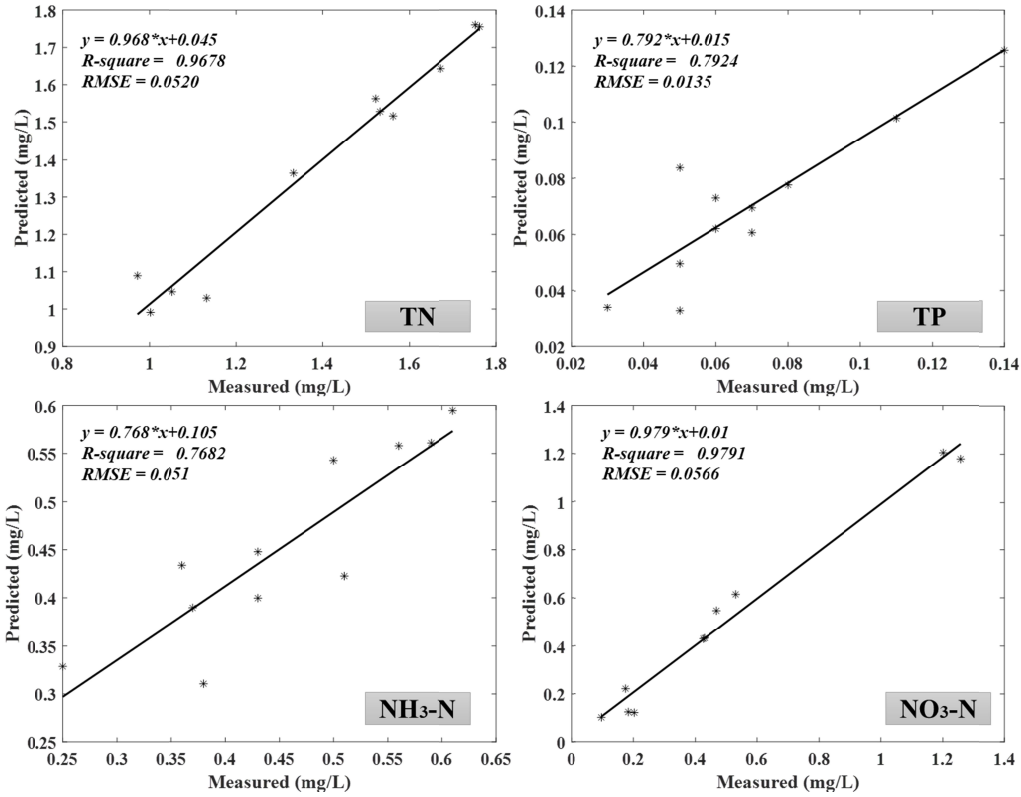
	TN (mg/L)	TP (mg/L)	NH_3 -N (mg/L)	NO_3 -N (mg/L)
Maximum	2.192	0.14	1.45	1.257
Minimum	0.972	0.03	0.25	0.001
Mean	1.457	0.075	0.537	0.415
Standard deviation	0.371	0.034	0.307	0.42

202 **B. Model Performance based on OHS and Sentinel-2**

203 As shown in Table 3, the polynomial model had the best accuracy for modeling TN, TP,
 204 NH₃-N, and NO₃-N concentrations based on OHS, and their R² was 0.9678, 0.7924, 0.7682 and
 205 0.9791, the corresponding RMSE was 0.0520 mg/L, 0.0135 mg/L, 0.051 mg/L and 0.0566 mg/L.
 206 The combination of green/NIR and Red edge1/NIR bands exhibited significant relationships with
 207 TN. The combination of NIR(940nm)/NIR(820nm) and NIR(806nm)/NIR(926nm) bands
 208 exhibited significant relationships with TP. The combination of Red edge1/NIR and Red
 209 edge2/Red bands exhibited significant relationships with NH₃-N. The combination of
 210 Red(596nm)/Red(665nm) and Blue/Red bands exhibited significant relationships with NO₃-N.
 211 From Figure 3, a strong linear relationship was shown between the measured and the predicted
 212 concentrations of TN, TP, NH₃-N and NO₃-N, which also indicated that polynomial model had
 213 good prediction accuracy and was appropriate for OHS remote sensing inversion.

214 Table 3 Statistics (R² and RMSE) for TN, TP, NH₃-N and NO₃-N concentrations based on OHS image.

	Model	Band ratio	R ²	RMSE (mg/L)
TN	Linear	B03/B05	0.6897	0.1616
	Exp	B02/B09	0.6946	0.1603
	Log	B03/B05	0.6892	0.1617
	Polynomial	B05/B24、 B16/B23	0.9678	0.0520
TP	Linear	B24/B23	0.4028	0.0228
	Exp	B24/B23	0.4159	0.0226
	Log	B24/B23	0.3898	0.0231
	Polynomial	B32/B24、 B23/B31	0.7924	0.0135
NH ₃ -N	Linear	B23/B21	0.3055	0.0883
	Exp	B25/B27	0.3479	0.0856
	Log	B03/B05	0.2923	0.0891
	Polynomial	B17/B23、 B19/B11	0.7682	0.051
NO ₃ -N	Linear	B10/B16	0.7458	0.1974
	Exp	B10/B16	0.757	0.193
	Log	B10/B16	0.7356	0.2013
	Polynomial	B10/B13、 B02/B09	0.9791	0.0566



216

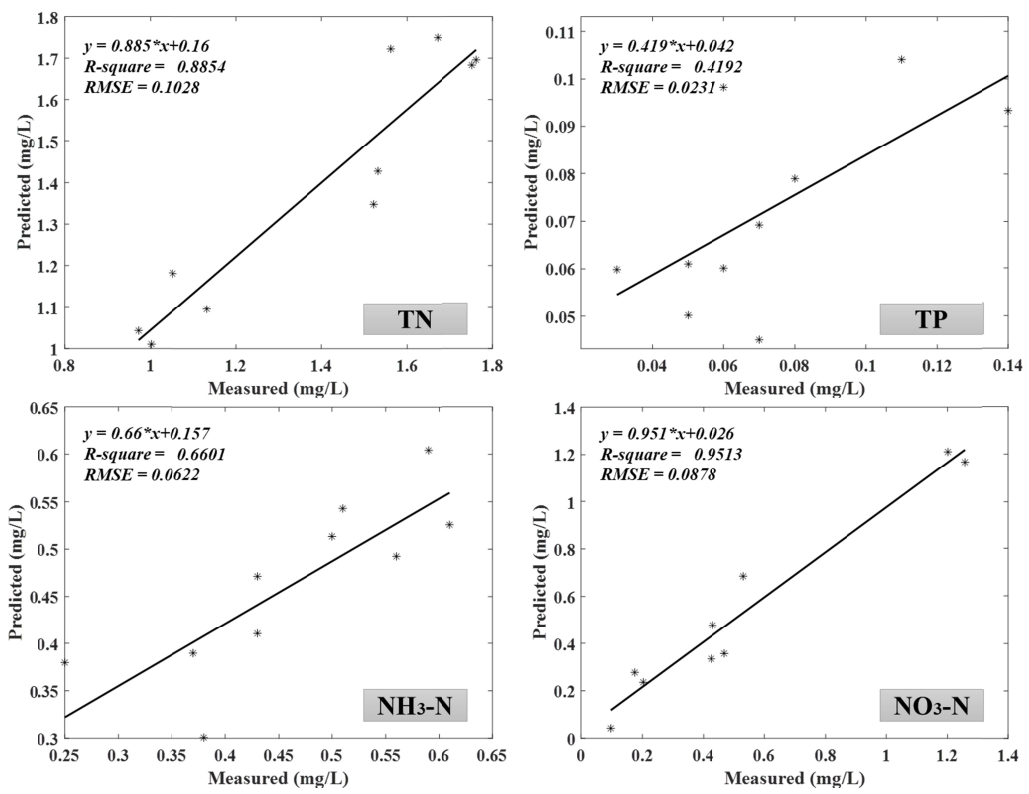
218 Figure 3 Accuracy of linear relationship between measured and predicted concentrations and RMSE of TN, TP,
 219 NH₃-N and NO₃-N from OHS image.

230 Compared to water quality estimation results using OHS images, a significant decrease
 231 performance was shown from Sentinel-2 image. It can be seen from Table 4 that the polynomial
 232 model had the best accuracy for modeling TN, TP, NH₃-N, and NO₃-N concentrations based on
 233 Sentinel-2, and their R² was 0.8854, 0.4192, 0.6601 and 0.9513, the corresponding RMSE was
 234 0.1028 mg/L, 0.0231 mg/L, 0.0622 mg/L and 0.0878 mg/L. The combination of NIR/Narrow NIR
 235 and Red edge1/Red bands exhibited significant relationships with TN. The combination of Red
 236 edge3/Blue and SWIR1/Blue bands exhibited significant relationships with NO₃-N. From Figure 4,
 237 a strong linear relationship was shown between the measured and the predicted concentrations of
 238 TN and NO₃-N, which indicated that polynomial model had good prediction accuracy and was
 239 appropriate for TN and NO₃-N inversion from Sentinel-2 images. However, we can also observe
 240 that there was a large difference between the predicted value and the observed value of TP and
 241 NH₃-N, indicating that the prediction errors are relatively large.

231 Table 4 Statistics (R² and RMSE) for TN, TP, NH₃-N and NO₃-N concentrations based on Sentinel-2 image.

	Model	Band ratio	R ²	RMSE (mg/L)
TN	Linear	b7/b8	0.8156	0.1304
	Exp	b7/b8	0.8173	0.1298
	Log	b7/b8	0.8138	0.1310
	Polynomial	b8/b8a, b5/b4	0.8854	0.1028

TP	Linear	b4/b2	0.1168	0.0284
	Exp	b4/b2	0.1195	0.0284
	Log	b4/b2	0.1133	0.0285
	Polynomial	b6/b8a、b8a/b2	0.4192	0.0231
NH ₃ -N	Linear	b4/b3	0.4156	0.0816
	Exp	b4/b3	0.4159	0.0815
	Log	b4/b3	0.4150	0.0816
	Polynomial	b6/b7、b4/b3	0.6601	0.0622
NO ₃ -N	Linear	b8a/b11	0.3112	0.3301
	Exp	b2/b12	0.3474	0.3213
	Log	b8a/b11	0.2978	0.3333
	Polynomial	b7/b2、b11/b2	0.9513	0.0878



232

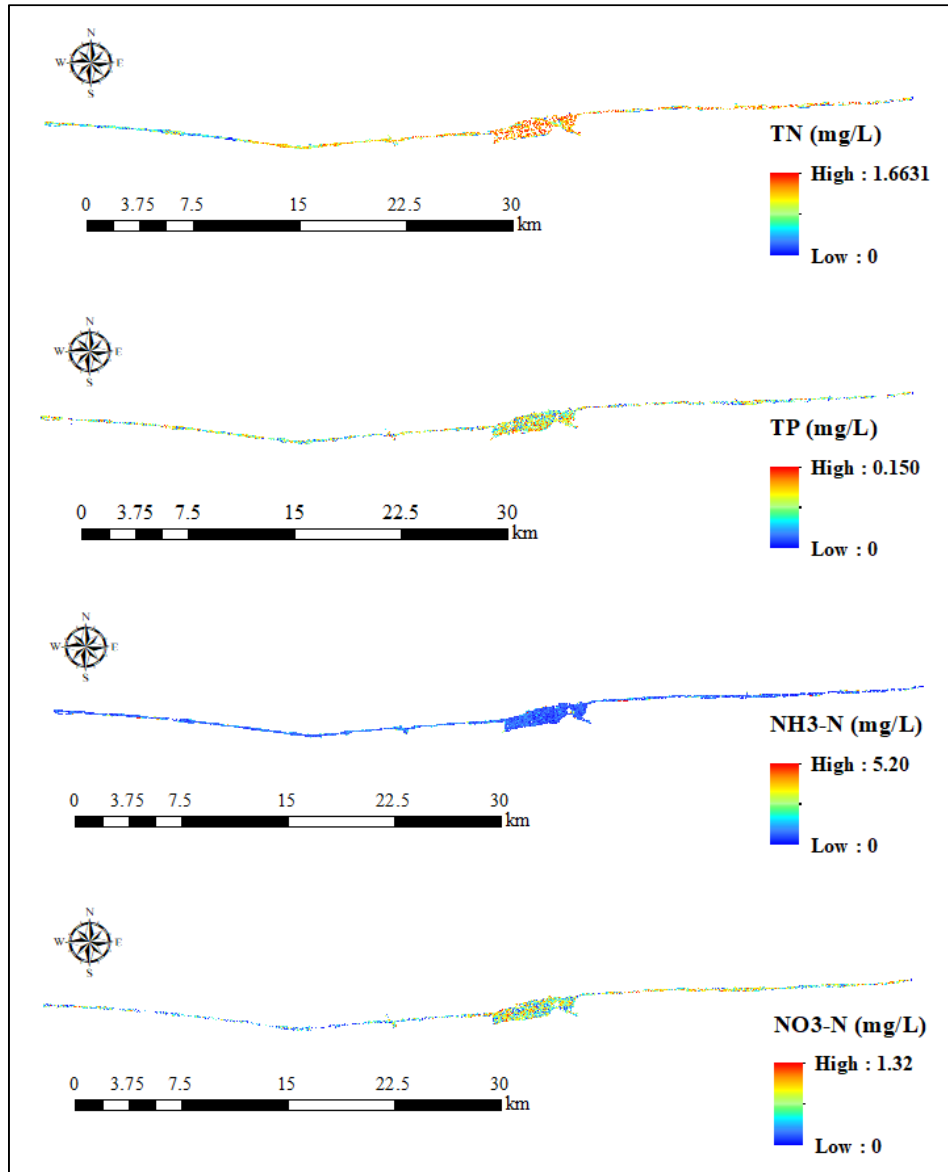
234 Figure 4 Accuracy of linear relationship between measured and predicted concentrations and RMSE of TN, TP,
 235 NH₃-N and NO₃-N from Sentinel-2 image.

235 **C. Optimal Model Application in Best-performed Images**

238 Figure 5 shows the results of TN, TP, NH₃-N and NO₃-N inversion of OHS image in the
 239 Taipu River using the best fitting model (polynomial). An obvious weakness of the polynomial
 240 model is that the negative and anomaly positive value will exist in the result. Therefore, the

238 inversion results exclude negative values and values outside the 95th percentile. The inversion
239 results showed that the maximum value of TN in the Taipu River is 1.66 mg/L, and the minimum
240 value is 0.0067 mg/L, which is basically consistent with the in-situ measurements (TN max =
241 2.192 mg/L, TN min = 0.972 mg/L). The maximum value of TP in the Taipu River is 0.15 mg/L,
242 and the minimum value is 0.001 mg/L, which is basically consistent with the in-situ measurements
243 (TP max = 0.14 mg/L, TP min = 0.03 mg/L). The maximum value of NH₃-N in the Taipu River is
244 5.2 mg/L, and the minimum value is 0.001 mg/L, which is higher than in-situ measurements
245 (NH₃-N max = 1.45 mg/L, NH₃-N min = 0.25 mg/L). However, the mean value of NH₃-N is
246 0.7718 mg/L, which indicates the NH₃-N concentration is low in the Taipu River. The maximum
247 value of NO₃-N in the Taipu River is 1.32 mg/L, and the minimum value is 0.001 mg/L, which is
248 basically consistent with the in-situ measurements (NO₃-N max = 1.257 mg/L, NO₃-N min =
249 0.001 mg/L).

250 The spatial distribution of TN and NO₃-N shows a general trend of deterioration in the water
251 quality of the Taipu River from upstream to downstream. The TP and NH₃-N concentration in
252 Taipu River is evenly distributed. It also can be seen that the water quality parameter of TN in the
253 upper reaches is class III and in the lower reaches is class IV. Moreover, the water quality
254 parameter of TP is class III, and the water quality classification results for NH₃-N is class IV.



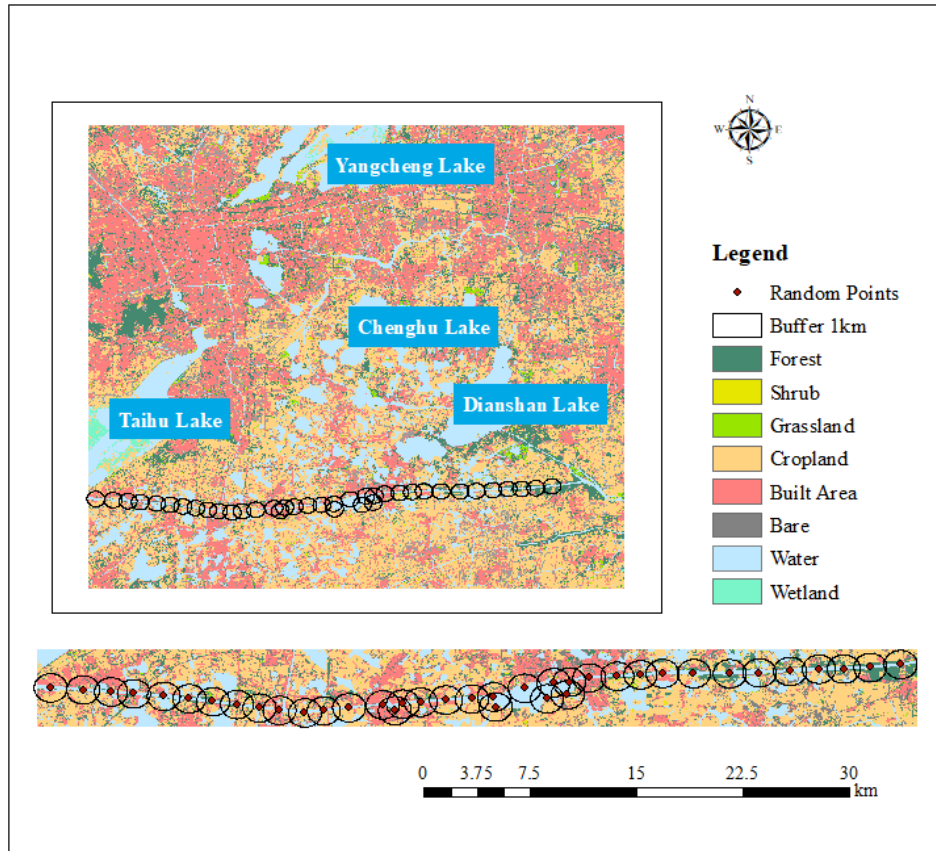
255

256 Figure 5 Spatial patterns of TN (a), TP (b), NH₃-N (c) and NO₃-N (d) in Taipu River.

257 **V. DISCUSSION**

258 **A. Driving Forces of Water Quality in the Taipu River**

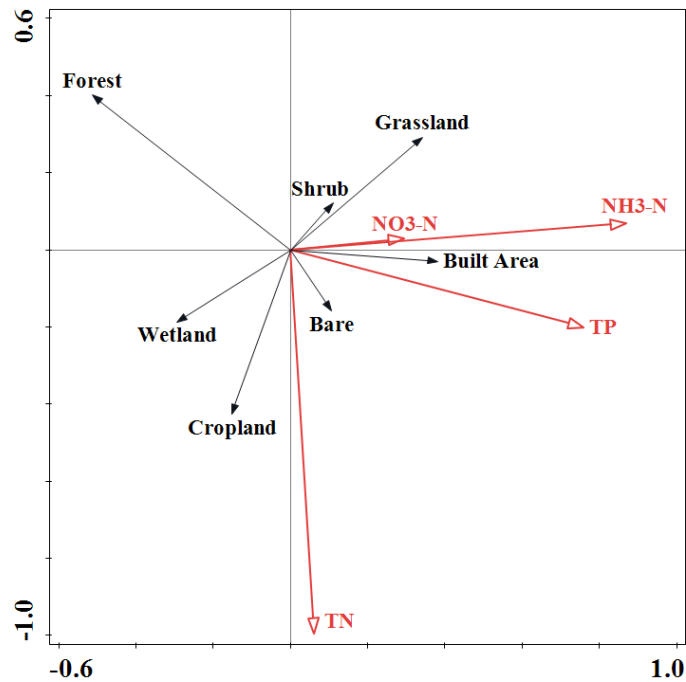
259 As the Figure 6 showed, the upper reaches of the Taipu River is occupied mainly by cropland;
 260 the middle reaches of the Taipu River is occupied mainly by impervious surface; the lower reaches
 261 of the Taipu River is dominated by forest. In this study, 38 random points was selected evenly
 262 distributed along the Taipu River to analyze the drivers of the water quality. The land cover
 263 percentage was calculated from 1km buffer.



264

265 Figure 6 1km buffer zones and land cover types in the Taipu River.

266 Diagrams derived from redundancy analysis using water quality parameters (red solid lines)
 267 and land cover metrics (black solid lines) from 1km buffers were shown in Figure 7. The angles
 268 between lines indicate the degree of correlation between individual variables, and the stronger the
 269 correlation, the smaller the angle. In addition, the acute angle between the two lines indicates a
 270 positive correlation, the obtuse angle indicates a negative correlation. The length of the lines
 271 represented the contribution of each land cover index to the water quality variables. Obviously, the
 272 narrow angles between TN and cropland indicated that cropland was primarily responsible for the
 273 negative effects on TN concentration. In particular, there has been a rise in the usage of herbicides
 274 and fertilizers in the last decades. Therefore, rapidly rising amounts of relevant pollutants have
 275 entered the river through precipitation and runoff (Xu et al., 2016). The narrow angles between
 276 three of the indicators (TP, NH₃-N, and NO₃-N) and built area indicated that built area was
 277 primarily responsible for the negative effects on TP, NH₃-N, and NO₃-N. Pollution from built area
 278 is a result of urban functions. Built-up areas are extremely likely to have a negative impact on the
 279 river's water quality due to the discharge of residential and industrial sewage (Wilson & Weng,
 280 2010). The large angle between the four water quality parameters and forest indicated that forest
 281 was primarily responsible for the beneficial effects on all the water quality parameters. Due to
 282 plant roots' capacity to absorb nitrogen, phosphorus, and organic matter, as well as soil microbes'
 283 ability to decompose organic matter, the forest has a good purifying effect on water quality than
 284 built area and cropland .



285

286 Figure 7 Redundancy analysis diagram in 1km buffer zones and proportion of land use/cover types in the Taipu
 287 River. (For interpretation of the references to colour in this figure legend, the reader is referred to the Web version
 288 of this article.)

289 **B. Sensitive Bands of Non-optical Parameters between OHS and Sentinel-2**

290 In recent years, hyperspectral technology has become increasingly mature, and it offers new
 291 options for water environmental monitoring. In hyperspectral remote sensing, spectral signatures
 292 are usually high dimensional, which supports the identification of elements or the measurement of
 293 concentrations (Krutz et al., 2019). Therefore, hyperspectral remote sensing technology is more
 294 suitable for complex inland bodies of water with non-optical characteristics. The OHS
 295 hyperspectral dataset which consists of 2.5nm spectral intervals, represents the target with
 296 continuous spectrum throughout the visible and NIR regions. It is more helpful for extracting the
 297 subtle spectral differences between water quality parameters (Zhang et al., 2021). In this study,
 298 Sentinel-2 and OHS were direct compared to provide more evidence on the potential of the
 299 hyperspectral data to retrieve water quality. By comparing the results in Table 3 and Table 4, it was
 300 found that the hyperspectral dataset generated higher accuracy models than the multispectral
 301 dataset in all cases. It is also shown that the feature bands of water quality retrieval were all
 302 comprise by ratio bands, which can reduce the impact of environmental factors to increase the
 303 accuracy of the analysis. The combination of green-NIR ratio and Red edge-NIR ratio were most
 304 sensitive to TN. The combination of NIR(940nm)-NIR(820nm) ratio and
 305 NIR(806nm)-NIR(926nm) ratio were most sensitive to TP. The combination of Red edge-NIR
 306 ratio and Red edge-Red ratio were most sensitive to NH₃-N. The combination of
 307 Red(596nm)-Red(665nm) ratio and R Blue-Red ratio were most sensitive to NO₃-N. It is also
 308 mentioned that the combination of Red edge-Blue ratio and SWIR1-Blue ratio derived from
 309 Sentinel-2 image also showed promising results of NO₃-N estimation. That means the SWIR

310 spectral region (OHS is not available) is critical for detecting NO₃-N concentration.

311 **C. Limitations of the Models**

312 The empirical method uses statistical regression models to link remotely sensed data (single
313 bands or band ratios) to in-situ water quality parameters. It is widely used in remote sensing
314 studies for inland water quality inversion, because it is simple and can be refined by selecting
315 more sensitive spectral bands to improve water quality retrieval accuracy(Li et al., 2017). The
316 results of empirical model indicated that TN、 TP、 NH₃-N and NO₃-N are highly correlated with
317 OHS spectral data with R² ranging from 0.76 to 0.79. The Artificial Intelligence (AI) mode (AIM)
318 concentrates on learning-from-data algorithms and, as a result, generates highly representative
319 features to make linear and non-linear predictions for new unseen data. AIM can also outperform
320 traditional empirical models, which rely heavily on band selection and band combinations. Many
321 researchers have used the AIM mode in water quality retrieval, such as neural networks (NN),
322 support vector machines (SVM), and deep learning (DL), and achieved relatively satisfying results
323 (Chebud et al., 2012; Leong et al., 2019; Pyo et al., 2019). Although the AIM has demonstrated
324 some apparent improvements in assessing water quality, there is an overfitting problem when the
325 sample is not adequate. The AIM cannot be employed in this study since the number of sampling
326 points is limited. The comparison between the empirical model and the AIM is put forward for
327 future research studies.

328 **VI. CONCLUSION**

329 Hyperspectral remote sensing, especially Zhuhai-1 satellite, is an emerging area for
330 monitoring non-optically active water quality parameters, which requires a significant amount of
331 investigation and development in terms of both methods and applications. In this study, we
332 examined four empirical models (linear, logarithmic, exponential and polynomial) for inversion of
333 water quality parameters from the newly available hyperspectral OHS imagery and Sentinel-2
334 imagery in Taipu River. The evaluation results indicated that OHS performed better than
335 Sentinel-2 for estimating TN, TP, NH₃-N and NO₃-N. This study also demonstrated that the
336 polynomial model based on band ratios performed best for estimating water quality parameters.
337 The band ratios of R(510)/R(820) and R(700)/R(806) performed the best retrieval of TN with R² =
338 0.9678. The band ratios of R(940)/R(820) and R(806)/R(926) performed the best retrieval of TP
339 with R² = 0.7924. The band ratios of R(709)/R(806) and R(746)/R(620) performed the best
340 retrieval of NH₃-N with R² = 0.7682. The band ratios of R(596)/R(665) and R(466)/R(580)
341 performed the best retrieval of NO₃-N with R² = 0.9791. It is worth mentioning that the band ratio
342 of Red Edge3/Blue and SWIR1/Blue of Sentinel-2 also performed well for NO₃-N inversion with
343 R² = 0.9513.

344 The OHS-based empirical models were found acceptable and applicable in estimating water
345 quality parameters of Taipu River. The spatial distribution of TN and NO₃-N shows a general trend
346 of deterioration in the water quality of the Taipu River from upstream to downstream. The TP and
347 NH₃-N concentration is evenly distributed, while all the values of water quality were relatively
348 low across the whole Taipu River. The RDA was applied to analyze the drivers of the spatial
349 distribution of water quality in the Taipu River. The results demonstrated that the proportion of
350 built-up area was significantly positively correlated with TP, NH₃-N and NO₃-N, and cropland was

351 significantly positively correlated with TN. The proportion of forest was significantly negatively
352 correlated with TN, TP, NH₃-N and NO₃-N. In future studies, the AI models will be investigated to
353 unlock the new opportunities of OHS data in large-scale area water quality inversion.

354 **CRedit authorship contribution statement**

355 Yukun Lin: Conceptualization, Methodology, Software, Writing – original draft, Writing –
356 review & editing, Project administration. Yaojen Tu: Conceptualization, Investigation, Resources,
357 Data Curation, Writing – Review & Editing. Wenpeng Lin: Conceptualization, Writing – review &
358 editing. Weiyue Li: Resources, Writing – Review & Editing. Qianwen Cheng: Software, Writing –
359 review & editing.

360 **Declaration of Competing Interest**

361 The authors declare that they have no known competing financial interests or personal
362 relationships that could have appeared to influence the work reported in this paper.

363 **Acknowledgments**

364 This work was supported by the National Natural Science Foundation of China [grant
365 number 41730642], the Central Guidance on Local Science and Technology Development Fund of
366 Shanghai [grant number YDZX20213100002003] and the Shanghai Natural Science Foundation
367 [grant number 20ZR1441100].

368 **References**

- 369 Arıman, S. (2021). Determination of inactive water quality variables by MODIS data: A case study in
370 the Kızılırmak Delta-Balik Lake, Turkey. *Estuarine, Coastal and Shelf Science*, 260, 107505.
371 <https://doi.org/https://doi.org/10.1016/j.ecss.2021.107505>
- 372 Cao, Q., Yu, G., Sun, S., Dou, Y., Li, H., & Qiao, Z. (2022). Monitoring Water Quality of the Haihe
373 River Based on Ground-Based Hyperspectral Remote Sensing. In *Water* (Vol. 14, Issue 1).
374 <https://doi.org/10.3390/w14010022>
- 375 Cao, Y., Ye, Y., Zhao, H., Jiang, Y., Wang, H., Shang, Y., & Wang, J. (2018). Remote sensing of
376 water quality based on HJ-1A HSI imagery with modified discrete binary particle swarm
377 optimization-partial least squares (MDBPSO-PLS) in inland waters: A case in Weishan Lake.
378 *Ecological Informatics*, 44, 21–32. <https://doi.org/https://doi.org/10.1016/j.ecoinf.2018.01.004>
- 379 Chebud, Y., Naja, G. M., Rivero, R. G., & Melesse, A. M. (2012). Water Quality Monitoring Using
380 Remote Sensing and an Artificial Neural Network. *Water, Air, & Soil Pollution*, 223(8), 4875–
381 4887. <https://doi.org/10.1007/s11270-012-1243-0>
- 382 Chen, B. T., Mu, X., Chen, P., Wang, B. A., Choi, J., Park, H., Xu, S., Wu, Y. L., & Yang, H. (2021).
383 Machine learning-based inversion of water quality parameters in typical reach of the urban river
384 by UAV multispectral data. *ECOLOGICAL INDICATORS*, 133.
385 <https://doi.org/10.1016/j.ecolind.2021.108434>
- 386 Chen, X., Wang, Y., Ye, C., Zhou, W., Cai, Z., Yang, H., & Han, X. (2018). Atmospheric Nitrogen
387 Deposition Associated with the Eutrophication of Taihu Lake. *Journal of Chemistry*, 2018,
388 4017107. <https://doi.org/10.1155/2018/4017107>

-
- 389 Donchyts, G., Schellekens, J., Winsemius, H., Eisemann, E., & Van de Giesen, N. (2016). A 30 m
390 Resolution Surface Water Mask Including Estimation of Positional and Thematic Differences
391 Using Landsat 8, SRTM and OpenStreetMap: A Case Study in the Murray-Darling Basin,
392 Australia. In *Remote Sensing* (Vol. 8, Issue 5). <https://doi.org/10.3390/rs8050386>
- 393 Dong, G., Hu, Z., Liu, X., Fu, Y., & Zhang, W. (2020). Spatio-Temporal Variation of Total Nitrogen
394 and Ammonia Nitrogen in the Water Source of the Middle Route of the South-To-North Water
395 Diversion Project. *WATER*, *12*(9). <https://doi.org/10.3390/w12092615>
- 396 Guo, H., Tian, S., Jeanne Huang, J., Zhu, X., Wang, B., & Zhang, Z. (2022). Performance of deep
397 learning in mapping water quality of Lake Simcoe with long-term Landsat archive. *ISPRS*
398 *Journal of Photogrammetry and Remote Sensing*, *183*, 451–469.
399 <https://doi.org/https://doi.org/10.1016/j.isprsjprs.2021.11.023>
- 400 Guo, H. W., Huang, J. J., Chen, B. W., Guo, X. L., & Singh, V. P. (2021). A machine learning-based
401 strategy for estimating non-optically active water quality parameters using Sentinel-2 imagery.
402 *INTERNATIONAL JOURNAL OF REMOTE SENSING*, *42*(5), 1841–1866.
403 <https://doi.org/10.1080/01431161.2020.1846222>
- 404 Huete, A., Didan, K., Miura, T., Rodriguez, E. P., Gao, X., & Ferreira, L. G. (2002). Overview of the
405 radiometric and biophysical performance of the MODIS vegetation indices. *Remote Sensing of*
406 *Environment*, *83*(1–2), 195–213.
- 407 Irish, R. R., Barker, J. L., Goward, S. N., & Arvidson, T. (2006). Characterization of the Landsat-7
408 ETM+ automated cloud-cover assessment (ACCA) algorithm. *Photogrammetric Engineering &*
409 *Remote Sensing*, *72*(10), 1179–1188.
- 410 Kallio, K., Kutser, T., Hannonen, T., Koponen, S., Pulliainen, J., Vepsäläinen, J., & Pyhälähti, T.
411 (2001). Retrieval of water quality from airborne imaging spectrometry of various lake types in
412 different seasons. *Science of The Total Environment*, *268*(1), 59–77.
413 [https://doi.org/https://doi.org/10.1016/S0048-9697\(00\)00685-9](https://doi.org/https://doi.org/10.1016/S0048-9697(00)00685-9)
- 414 Krutz, D., Müller, R., Knodt, U., Günther, B., Walter, I., Sebastian, I., Säuberlich, T., Reulke, R.,
415 Carmona, E., Eckardt, A., Venus, H., Fischer, C., Zender, B., Arloth, S., Lieder, M., Neidhardt,
416 M., Grote, U., Schrandt, F., Gelmi, S., & Wojtkowiak, A. (2019). The Instrument Design of the
417 DLR Earth Sensing Imaging Spectrometer (DESI). In *Sensors* (Vol. 19, Issue 7).
418 <https://doi.org/10.3390/s19071622>
- 419 Leong, W. C., Bahadori, A., Zhang, J., & Ahmad, Z. A. (2019). Prediction of water quality index (WQI)
420 using support vector machine (SVM) and least square-support vector machine (LS-SVM).
421 *International Journal of River Basin Management*, *19*, 149–156.
- 422 Li, Y., Zhang, Y., Shi, K., Zhu, G., Zhou, Y., Zhang, Y., & Guo, Y. (2017). Monitoring spatiotemporal
423 variations in nutrients in a large drinking water reservoir and their relationships with hydrological
424 and meteorological conditions based on Landsat 8 imagery. *Science of The Total Environment*,
425 *599–600*, 1705–1717. <https://doi.org/https://doi.org/10.1016/j.scitotenv.2017.05.075>
- 426 Liang, Z., Chen, H., Wu, S., Zhang, X., Yu, Y. H., & Liu, Y. (2018). Exploring Dynamics of the
427 Chlorophyll a-Total Phosphorus Relationship at the Lake-Specific Scale: a Bayesian Hierarchical

-
- 428 Model. *Water, Air, and Soil Pollution*, 229(1). <https://doi.org/10.1007/s11270-017-3678-9>
- 429 Liu, C., Qian, B. J., Wang, L. Y., & Mao, Q. (2019). Application of GIS and Remote Sensing in Spatial
430 Distribution of Nitrogen and Phosphorus Pollutant in Urban Rivers: A Case Study of Linyi
431 Economic Development Zone, China. *JOURNAL OF COASTAL RESEARCH*, 250–256.
432 <https://doi.org/10.2112/SI93-033.1>
- 433 Liu, J., Zhang, Y., Yuan, D., & Song, X. (2015). Empirical Estimation of Total Nitrogen and Total
434 Phosphorus Concentration of Urban Water Bodies in China Using High Resolution IKONOS
435 Multispectral Imagery. In *Water* (Vol. 7, Issue 11, pp. 6551–6573).
436 <https://doi.org/10.3390/w7116551>
- 437 Lv, J., & Wu, Y. (2021). Nitrogen removal by different riparian vegetation buffer strips with different
438 stand densities and widths. *Water Supply*, 21(7), 3541–3556. <https://doi.org/10.2166/ws.2021.119>
- 439 Mararakanye, N., Le Roux, J. J., & Franke, A. C. (2022). Long-term water quality assessments under
440 changing land use in a large semi-arid catchment in South Africa. *Science of The Total
441 Environment*, 818, 151670. <https://doi.org/https://doi.org/10.1016/j.scitotenv.2021.151670>
- 442 Marshak, C., Simard, M., Denbina, M., Nilsson, J., & Van der Stocken, T. (2020). Orinoco: Retrieving
443 a River Delta Network with the Fast Marching Method and Python. In *ISPRS International
444 Journal of Geo-Information* (Vol. 9, Issue 11). <https://doi.org/10.3390/ijgi9110658>
- 445 Pyo, J., Duan, H., Baek, S., Kim, M. S., Jeon, T., Kwon, Y. S., Lee, H., & Cho, K. H. (2019). A
446 convolutional neural network regression for quantifying cyanobacteria using hyperspectral
447 imagery. *Remote Sensing of Environment*, 233, 111350.
448 <https://doi.org/https://doi.org/10.1016/j.rse.2019.111350>
- 449 Qin, P., Cai, Y., & Wang, X. (2022). Small Waterbody Extraction With Improved U-Net Using
450 Zhuhai-1 Hyperspectral Remote Sensing Images. *IEEE Geoscience and Remote Sensing Letters*,
451 19, 1–5.
- 452 Qiu, S., Zhu, Z., & He, B. (2019). Fmask 4.0: Improved cloud and cloud shadow detection in Landsats
453 4-8 and Sentinel-2 imagery. *Remote Sensing of Environment*.
- 454 Ross, M. R. V., Topp, S. N., Appling, A. P., Yang, X., Kuhn, C., Butman, D., Simard, M., & Pavelsky,
455 T. M. (2019). AquaSat: A Data Set to Enable Remote Sensing of Water Quality for Inland
456 Waters. *Water Resources Research*, 55(11), 10012–10025.
457 <https://doi.org/https://doi.org/10.1029/2019WR024883>
- 458 Shi, J., Shen, Q., Yao, Y., Li, J., Chen, F., Wang, R., Xu, W., Gao, Z., Wang, L., & Zhou, Y. (2022).
459 Estimation of Chlorophyll-a Concentrations in Small Water Bodies: Comparison of Fused
460 Gaofen-6 and Sentinel-2 Sensors. *Remote Sensing*, 14(1). <https://doi.org/10.3390/rs14010229>
- 461 Shi, K., Zhang, Y., Zhu, G., Qin, B., & Pan, D. (2018). Deteriorating water clarity in shallow waters:
462 Evidence from long term MODIS and in-situ observations. *International Journal of Applied
463 Earth Observation and Geoinformation*, 68, 287–297.
464 <https://doi.org/https://doi.org/10.1016/j.jag.2017.12.015>
- 465 Song, K. S., Li, L., Tedesco, L., Li, S., Shi, K., & Hall, B. (2014). Remote Estimation of Nutrients for a

-
- 466 Drinking Water Source Through Adaptive Modeling. *WATER RESOURCES MANAGEMENT*,
467 28(9), 2563–2581. <https://doi.org/10.1007/s11269-014-0627-x>
- 468 Sun, D., Qiu, Z., Li, Y., Shi, K., & Gong, S. (2014). Detection of Total Phosphorus Concentrations of
469 Turbid Inland Waters Using a Remote Sensing Method. *Water, Air, & Soil Pollution*, 225(5),
470 1953. <https://doi.org/10.1007/s11270-014-1953-6>
- 471 Sun, X., Zhang, Y., Shi, K., Zhang, Y., Li, N., Wang, W., Huang, X., & Qin, B. (2022). Monitoring
472 water quality using proximal remote sensing technology. *Science of The Total Environment*, 803,
473 149805. <https://doi.org/https://doi.org/10.1016/j.scitotenv.2021.149805>
- 474 Toming, K., Kutser, T., Laas, A., Sepp, M., Paavel, B., & Nõges, T. (2016). First Experiences in
475 Mapping Lake Water Quality Parameters with Sentinel-2 MSI Imagery. *Remote Sensing*, 8(8).
476 <https://doi.org/10.3390/rs8080640>
- 477 Wang, S., Shen, M., Liu, W., Ma, Y., Shi, H., Zhang, J., & Liu, D. (2022). Developing remote sensing
478 methods for monitoring water quality of alpine rivers on the Tibetan Plateau. *GIScience &*
479 *Remote Sensing*, 59(1), 1384–1405. <https://doi.org/10.1080/15481603.2022.2116078>
- 480 Wang, X. L., Fu, L., & He, C. S. (2011). Applying support vector regression to water quality modelling
481 by remote sensing data. *INTERNATIONAL JOURNAL OF REMOTE SENSING*, 32(23), 8615–
482 8627. <https://doi.org/10.1080/01431161.2010.543183>
- 483 Wang, Y., He, B., Duan, W., Li, W., Luo, P., & Razafindrabe, B. H. N. (2016). Source apportionment
484 of annual water pollution loads in river basins by remote-sensed land cover classification. *Water*
485 *(Switzerland)*, 8(9), 1–14. <https://doi.org/10.3390/w8090361>
- 486 Wang, Y., Li, F., Mao, L., Chen, M., Tao, H., & Li, J. (2021). Spatial Distribution and Pollution
487 Assessment of Potentially Toxic Elements (PTEs) in Surface Sediments at the Drinking Water
488 Source Channel of Taipu River in China. In *Minerals* (Vol. 11, Issue 11).
489 <https://doi.org/10.3390/min11111202>
- 490 Wang, Z., Wei, L., He, C., & Lu, Q. (2021). Ammonia Nitrogen Monitoring of Urban Rivers with
491 UAV-Borne Hyperspectral Remote Sensing Imagery. *2021 IEEE International Geoscience and*
492 *Remote Sensing Symposium IGARSS*, 3713–3716.
493 <https://doi.org/10.1109/IGARSS47720.2021.9554632>
- 494 Wilson, C., & Weng, Q. (2010). Assessing Surface Water Quality and Its Relation with Urban Land
495 Cover Changes in the Lake Calumet Area, Greater Chicago. *Environmental Management*, 45(5),
496 1096–1111. <https://doi.org/10.1007/s00267-010-9482-6>
- 497 Xu, J., Li, Z., Chi, H., Wang, M., Guan, C., Reiff-Marganiec, S., & Shen, H. (2016). Optimized
498 Composite Service Transactions through Execution Results Prediction. *2016 IEEE International*
499 *Conference on Web Services (ICWS)*, 690–693. <https://doi.org/10.1109/ICWS.2016.107>
- 500 Yang, H., Kong, J., Hu, H., Du, Y., Gao, M., & Chen, F. (2022). A Review of Remote Sensing for
501 Water Quality Retrieval: Progress and Challenges. In *Remote Sensing* (Vol. 14, Issue 8).
502 <https://doi.org/10.3390/rs14081770>
- 503 Yang, X., Qin, Q., Grussenmeyer, P., & Koehl, M. (2018). Urban surface water body detection with

504 suppressed built-up noise based on water indices from Sentinel-2 MSI imagery. *Remote Sensing*
505 *of Environment*, 219(October), 259–270. <https://doi.org/10.1016/j.rse.2018.09.016>

506 Yao, H., Qian, X., Gao, H., Wang, Y., & Xia, B. (2014). Seasonal and Spatial Variations of Heavy
507 Metals in Two Typical Chinese Rivers: Concentrations, Environmental Risks, and Possible
508 Sources. In *International Journal of Environmental Research and Public Health* (Vol. 11, Issue
509 11, pp. 11860–11878). <https://doi.org/10.3390/ijerph111111860>

510 Yao, H., Qian, X., Yin, H., Gao, H., & Wang, Y. (2015). Regional Risk Assessment for Point Source
511 Pollution Based on a Water Quality Model of the Taipu River, China. *RISK ANALYSIS*, 35(2),
512 265–277. <https://doi.org/10.1111/risa.12259>

513 Zhang, X. W., Zhang, J. C., Chen, W. Y., Liu, W., Zhang, Z. J., Fan, J. W., Xiao, C. J., & Wang, R.
514 (2021). Semi-automated extraction of surface water based on ZhuHai-1 hyperspectral satellite
515 images. *REMOTE SENSING LETTERS*, 12(8), 750–756.
516 <https://doi.org/10.1080/2150704X.2021.1934593>

517 Zhong, Y., Wang, X., Wang, S., & Zhang, L. (2021). Advances in spaceborne hyperspectral remote
518 sensing in China. *Geo-Spatial Information Science*, 24(1), 95–120.
519 <https://doi.org/10.1080/10095020.2020.1860653>

520 Zhu, H. (2018). Distribution and control countermeasures for antimony in water source of Huangpu
521 River upper stream. *Water Purif. Technol*, 37, 25–32.

522 Zhu, Z., Wang, S., & Woodcock, C. E. (2015). Improvement and expansion of the Fmask algorithm:
523 cloud, cloud shadow, and snow detection for Landsats 4–7, 8, and Sentinel 2 images. *Remote*
524 *Sensing of Environment*, 159, 269–277. <https://doi.org/https://doi.org/10.1016/j.rse.2014.12.014>

525